



In-situ acoustic emission study of Si-based electrodes for Li-ion batteries



A. Tranchot^{a, b}, A. Etienne^{a, b}, P.-X. Thivel^c, H. Idrissi^{b, *}, L. Roué^{a, **}

^a INRS – Énergie, Matériaux, Télécommunications, Varennes, Québec J3X 1S2, Canada

^b INSA-Lyon, MATEIS CNRS UMR5510, F-69621 Villeurbanne, France

^c Université Grenoble Alpes, CNRS, LEPMI, F-38000 Grenoble, France

HIGHLIGHTS

- The mechanical degradation of a Si-based electrode is studied by acoustic emission.
- Three distinctive populations of acoustic signals are identified.
- Acoustic signals are mainly detected during the first lithiation.
- Si particle cracking is initiated in the early stage of the lithiation.
- The electrode cracking is accentuated by the formation of the c-Li₁₅Si₄ phase.

ARTICLE INFO

Article history:

Received 15 November 2014

Received in revised form

23 December 2014

Accepted 25 December 2014

Available online 26 December 2014

Keywords:

Li-ion battery

Si-based anode

Acoustic emission

Signal clustering

Fracture detection

ABSTRACT

The mechanical degradation of a Si powder (~2 μm) based electrode is investigated by acoustic emission (AE). AE signals are mainly detected during the first lithiation, suggesting that electrode cracking mainly occurs during this period. The formation of the solid electrolyte interface (SEI) is not very acoustically emissive, in contrast to the Si particle cracking which is initiated in the early stage of the lithiation in accordance with a core–shell lithiation mechanism. An increase of the AE activity is observed at the end of the discharge when the c-Li₁₅Si₄ phase is formed and during the charge when the potential reaches ~0.45 V, corresponding to the delithiation of c-Li₁₅Si₄. From a clustering procedure, three types of signals are identified: type-1 signals consisting of a succession of very short waveforms with high peak frequency (~700 kHz) are primarily detected when the Si lithiation is initiated and are ascribed to the nucleation of surface microcracks on the Si particles; type-2 signals (peak frequency ~400 kHz), present all during the Si lithiation, are attributed to the propagation of cracks through the Si particles and into the composite film; type-3 signals (peak frequency ~200 kHz), detected when the potential reaches 60 mV, are ascribed to the accentuation of the electrode cracking due to the c-Li₁₅Si₄ formation.

© 2014 Elsevier B.V. All rights reserved.

1. Introduction

Li-ion batteries have adequate performance for most portable electronic devices but for new applications such as electric vehicles, it is crucial to raise their energy density. Replacing the graphite in the negative electrode by an active material such as silicon would be extremely beneficial since the specific capacity of silicon

(3578 mAh g⁻¹) is about ten times higher than that of carbon (372 mAh g⁻¹). Nonetheless, upon lithiation, silicon undergoes an important volume expansion, up to 280%, to form Li₁₅Si₄ [1]. By comparison, graphite expands by only 10% when LiC₆ is formed. Such a huge volume variation causes significant cracking of the Si particles and the composite film, leading to a loss of electrical contact [2]. Furthermore, it induces an instability of the solid electrolyte interface (SEI), which continuously grows on the silicon surface with cycling, inducing a low coulombic efficiency in addition to increase the electrode polarization resistance [3,4].

Post mortem analyses by scanning electron microscopy (SEM) or transmission electron microscopy (TEM) do not allow a detailed analysis of the Si cracking process, which can vary significantly

* Corresponding author.

** Corresponding author. INRS-Énergie, Matériaux et Télécommunications, 1650, bd. Lionel Boulet, Varennes, Québec J3X1S2, Canada.

E-mail addresses: hassane.idrissi@insa-lyon.fr (H. Idrissi), roue@emt.inrs.ca (L. Roué).

depending on the electrode composition and processing, and the charge/discharge conditions. This is a key issue for the development of more efficient Si-based anodes. In this context, acoustic emission (AE) appears as a relevant characterization tool. The AE technique is based on the fact that, when undergoing mechanical modification, even at a local level, materials can spontaneously generate transient elastic waves, called acoustic emission, allowing the detection of active defaults within materials on a real-time and continuous basis during the test. AE has been used since the 70's in industries for the detection of defaults (fracture, leaks ...) and surveillance on large structure [5]. Recently, it has been shown that AE can also be used for *in situ* monitoring of the degradation of battery electrodes such as metal hydride electrodes for Ni–MH batteries [6,7] and various electrodes for Li-ion batteries, e.g. MnO_2 [8], graphite [9,10], NiSb_2 [11], Al [12] and Si [13–15]. In these various studies, cracking of the active material, gas evolution and/or SEI formation are the main sources of AE signals.

Regarding Si-based electrodes, Rhodes et al. have shown that the major source of AE events is the surface fracture of the Si particles (~130 μm in size), which mainly occurs during the first lithiation [13]. In the present study, a more detailed analysis of the AE signals detected during the cycling of a Si-based electrode constituted of smaller particles (~2 μm in size) is performed by clustering the AE signals in distinctive populations according to their acoustic characteristics. On the basis of these results, complemented by SEM and electrochemical data, the origin of the different AE signals detected upon electrode cycling is discussed with the aim to clarify the electrode degradation process.

2. Experimental

2.1. Electrode preparation

The composite electrode was made using micrometric silicon (Alfa Aesar, 99.9%, 1–5 μm) as active material, Timcal Super P carbon black (CB) as conductive agent, and carboxymethyl cellulose (CMC) (Aldrich, DS = 0.7, Mw = 90,000) as binder. A mixture of 200 mg of Si + CB + CMC in a weight proportion of 80:12:8 was introduced along with 0.5 mL of a buffer solution at pH 3 (citric acid + KOH) and three silicon nitride balls into a silicon nitride vial. Mixing was performed at 500 rpm for 1 h using a Fritsch Pulverisette 7 mixer. As previously shown [16], the buffering at pH 3 promotes covalent bonding (esterification) between –OH groups present on the surface of Si particles and –COOH groups of CMC, which significantly improves the electrode cycle life. The slurry was then tape cast without calendar pressure using a doctor blade onto a 25 μm thick copper foil, dried at room temperature for 12 h and then at 100 °C in vacuum for 2 h. The final weight composition of the electrode was 73.1% of Si, 11% of carbon, 7.3% of CMC and 8.6% of citric acid + KOH. The Si mass loading of the electrode was about 1 mg cm^{-2} and the deposit thickness was about 25 μm .

2.2. Material characterization

The as-received Si powder and pristine and cycled electrodes were characterized by scanning electron microscopy (SEM) using a Jeol JSM 6300F microscope. Before SEM analyses, the cycled electrodes were gently rinsed in DMC solvent in an Ar-filled glove box and dried under vacuum. The particle size distribution of the as-received Si powder was determined by the laser scattering method in an aqueous medium using a Mastersizer 2000 Malvern analyser.

2.3. Electrochemical-AE measurements

Electrochemical-AE experiments were performed at room temperature using a two-electrode Swagelok®-type cell as schematized in Fig. 1a. The cell was assembled in an argon-filled glove box and comprises: (i) a 1 cm diam. disc of the composite working electrode; (ii) a Whatman GF/D borosilicate glass-fiber separator soaked with electrolyte made of 1 M LiPF_6 in 1:1 in ethylene carbonate/dimethyl carbonate; and (iii) a 1 cm diam. Li metal disc as the counter and reference electrode. Electrodes were cycled at full capacity between 1 and 0.005 V (vs Li/Li^+) at a current density of 475 mA g^{-1} of Si using a VMP3 multichannel potentiostat/galvanostat (Bio-Logic, France).

The AE signals were recorded by a micro80 sensor (Mistras, operating frequency range 100–1000 kHz) fixed with silicone grease on the current collector of the working electrode (Fig. 1a). A polypropylene film (0.2 mm thick) was placed as current insulator between the AE sensor and the current collector. The AE signals were transmitted via a USB Node acquisition card (Mistras) to the computer. The AE acquisition parameters are listed in Table 1.

2.4. Acoustic signal analysis

The recorded acoustic signals were treated using AE Win software (Mistras). AE signals with a peak frequency lower than 80 kHz or less than 2 counts, considered as noise events, were eliminated. From the AE waveform, characteristic parameters of the AE signal can be extracted as illustrated in Fig. 1b, such as its amplitude, duration, count number, rise time, and energy. In addition, Fast Fourier Transform (FFT) of the AE signals was performed to determine their frequency components.

It is difficult to analyze a cloud of data when they are described

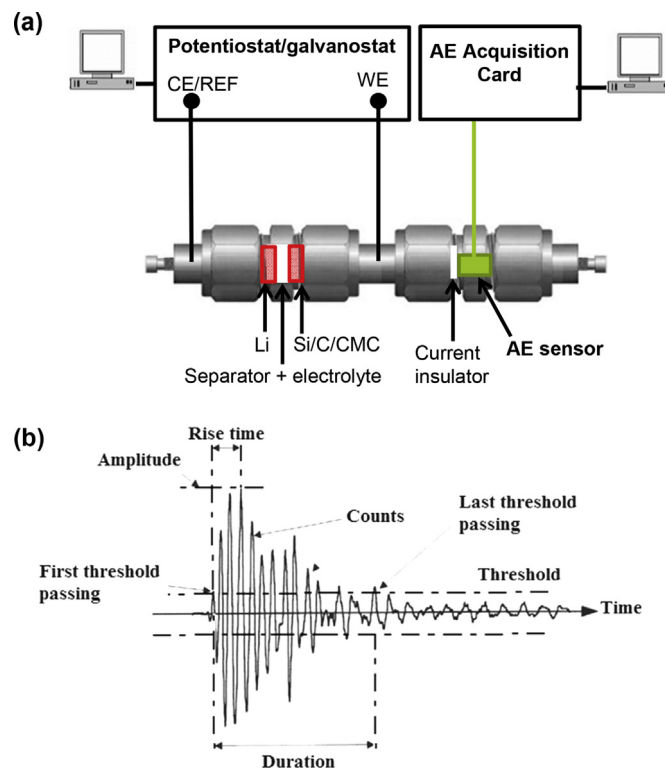


Fig. 1. (a) Schematic diagram of the experimental set-up coupling AE and electrochemical measurements. (b) Main acoustic characteristics recorded on a typical waveform AE signal.

Table 1
Acquisition parameters of the acoustic signals.

Pre amplification gain	40 dB
Threshold	27 dB
Analog filter	20 kHz–1 MHz
Length/Pre trigger/Sample rate	1 k dots/20 μ s/ 5 MHz
Peak definition time (PDT)/Hit definition time (HDT)/Hit lockout time (HLT)	300 μ s/600 μ s/ 800 μ s

by a large number of descriptors as AE signals. In this case, the Principal Component Analysis (PCA) [17] can be used to extract, compress and classify relevant information from complex AE data sets. The PCA procedure was performed by assimilating each AE hit to a vector, the coordinates of which correspond to the various AE parameters (amplitude, duration ...). The purpose is to reduce the dimensionality of an AE data set by finding a new set of variables, smaller than the original set. These new variables, called Principal Components (PC1, PC2 ...), are linear combinations of the acoustic parameters (the original set); therefore they have no physical meaning. Unsupervised clustering was then performed by a K-mean algorithm. This iterative technique separates the data by minimizing the variance within each cluster. The initial clusters were randomly selected, then each data point was assigned to a cluster using the nearest neighbor classification. Wilk's λ , R_{ij} and τ criteria were used to optimize the partition. Noesis software (Mistras) was used to perform the PCA and partition. In order to confirm and refine this statistical classification, a partition was then performed manually based on the visual inspection of the shape of the AE waveforms and corresponding power (FFT) spectra. As a result, the AE signals were classified in distinct populations with

the objective to facilitate their assignment to different phenomenon occurring upon Si electrode cycling.

3. Results and discussion

3.1. Si powder and electrode morphologies

A SEM micrograph of the as-received silicon powder (Fig. 2a) shows that the particles have an irregular plate-like shape. As shown in Fig. 2b, the particle size distribution is monomodal. 95% of the particles have a size below 4.5 μ m and their median size is 1.8 μ m.

Fig. 3 compares SEM micrographs of the electrode surface before cycling and after the 1st and 10th cycle at different magnifications. The pristine electrode (Fig. 3a) does not display any cracks. The large magnification micrograph shows that the electrode is rather porous. The Si particles are clearly discernable and seem to be well dispersed in the composite electrode. After the 1st discharge (Fig. 3b), cracks appear on the electrode surface (see the median magnification image) but they are not very discernable due to their small width. At larger magnification, a few fissures appear on the Si particles (spotted with arrows) but they are also hardly discernable. After the 1st charge (Fig. 3c), cracks on the film are much more visible, with a width as high as 10 μ m. Their enlargement can be explained by the volume contraction of the electrode during the delithiation process. As shown in the large magnification image in Fig. 3c, the Si particles are smaller in size (typically, $\leq 1 \mu$ m) than for the uncycled electrode (1–5 μ m, Fig. 3a), which tends to confirm their fracturing during the 1st cycle. However, intraparticle fissures are not very discernable in contrast to what was observed by Rhodes et al. on much larger Si particles ($\sim 130 \mu$ m in initial size) [13,14]. On the other hand, SEM observations on nanosized Si electrodes have shown that the morphology of the Si particles (200 nm in size) are nearly unmodified after 10 cycles, whereas the electrode film displays large cracks on its surface [18]. Besides, the fact that the Si and CB particles are much less distinguishable on the 1st discharge/charge electrodes (Fig. 3b and c, large magnification) compared to the pristine electrode (Fig. 3a) may be due to the presence of electrolyte (solvent) degradation products (e.g. Li_2CO_3) related to the SEI formation. By comparing Fig. 3c and d, no major difference in the electrode morphology is observed between the 1st and 10th cycle, suggesting that composite film cracking and Si particle fracturing mainly occur during the first cycle. Note that many micrometric grooves appear on the 10th cycle electrode (see low and median magnifications in Fig. 3d), which correspond to the imprint of the fibrous separator, probably resulting from the volume expansion of the Si electrode with cycling.

3.2. Evolution of the electrode capacity and acoustic activity with cycling

Fig. 4a shows typical evolution with cycling (first 10 cycles) of the electrode potential and cumulated acoustic activity (expressed in terms of number of AE hits per mg of Si). The evolution with cycling of the electrode capacity and AE activity (averaged on 8 experiments) is shown in Fig. 4b. The capacity of the first discharge (lithiation) is about 3200 mAh g^{-1} , which is close to the theoretical value (3578 mAh g^{-1}). This means that a large fraction ($\sim 90\%$) of the Si material is electrochemically accessible despite the fact that intensive Si particle fracturing occurs during the first discharge, as shown below from AE measurements. This may be due to the volume expansion of the Si particles, which helps to maintain a good contact between the fractured Si particles and the C additive. One must note that a small part of this discharge capacity (estimated at about 100 mAh g^{-1} , see Fig. 5) is also generated by the SEI

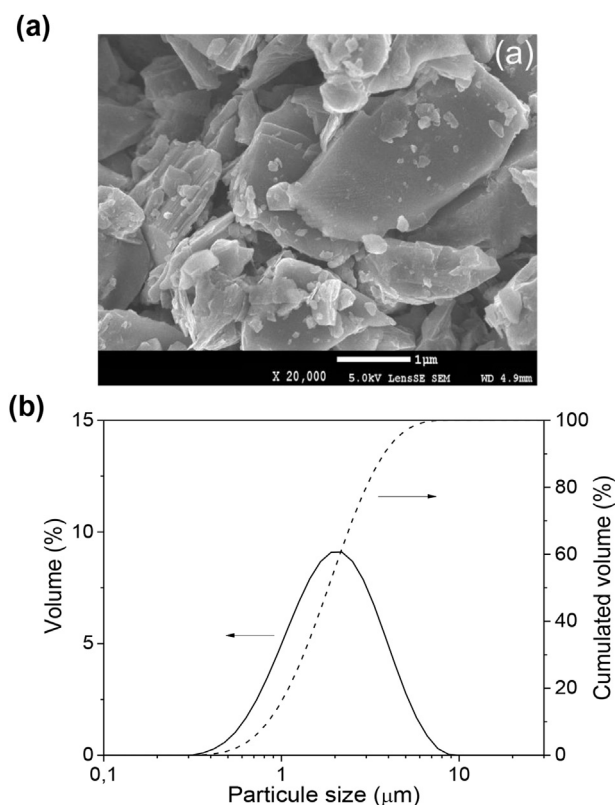


Fig. 2. (a) SEM micrographs and (b) particles size distribution of the as-received Si powder.

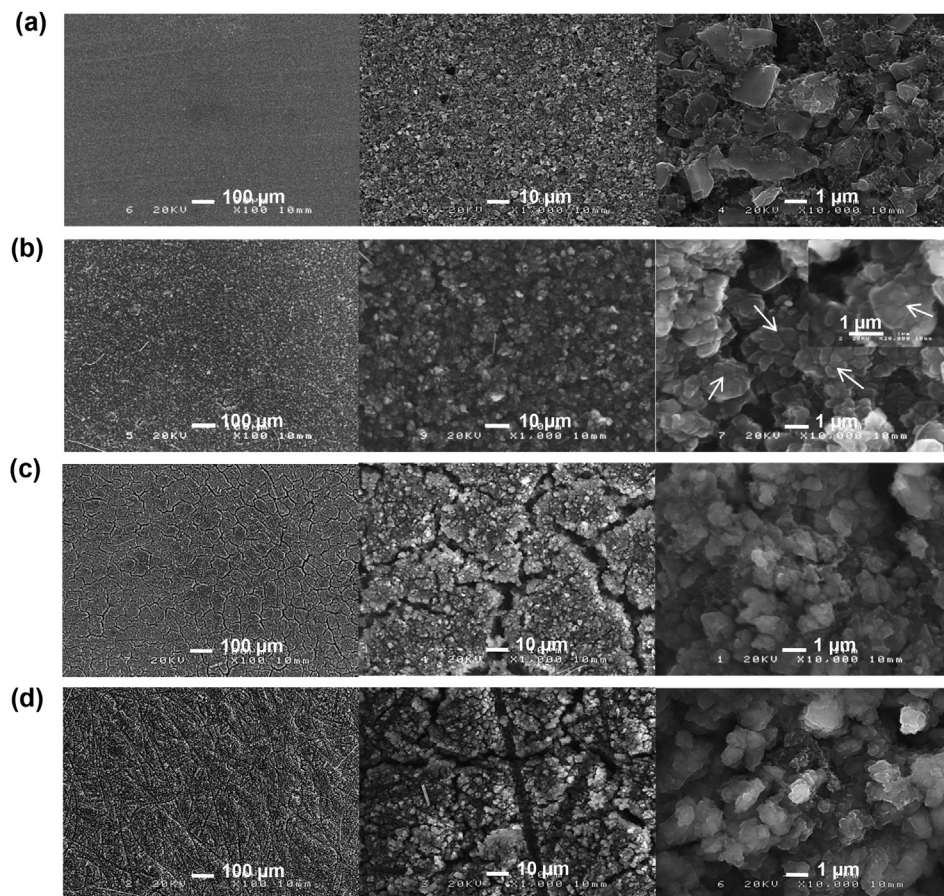


Fig. 3. SEM micrographs at different magnifications of the electrode surface (a) before cycling, (b) after the 1st discharge (lithiation), (c) after the 1st charge and (d) after the 10th cycle.

formation. This can explain the fact that the discharge capacity is always slightly higher than the charge capacity measured at each cycle, as displayed in Fig. 4. However, this difference is attenuated with cycling, suggesting that the SEI growth becomes less intensive, probably because fewer fresh Si surfaces are created. The first charge (delithiation) capacity is much lower (2500 mAh g^{-1}), which can be attributed to the electrical disconnection of some Si particles. Indeed, upon delithiation, the volume contraction of the Si particles may cause poor contact with carbon and/or the current collector and eventually the isolation of some Si particles from the electronic network [2]. This interpretation is supported by the presence of large cracks observed by SEM on the 1st charge electrode (Fig. 3c). From the 2nd cycle, the loss of capacity with cycling is much lower, with a nearly steady decay of 20 mAh g^{-1} per cycle compared to 700 mAh g^{-1} for the first cycle. This also agrees with the previous SEM observations showing that the degradation of the electrode morphology mainly occurs during the first cycle.

Regarding the evolution of the AE activity with cycling in Fig. 4b, AE events are mainly detected during the first discharge (~ 200 hits) then drastically decrease for the subsequent first charge (~ 40 hits) and following cycles (< 20 hits per cycle). A similar evolution of the AE activity with cycling was observed by Rhodes et al. on their Si-based electrodes with, however, a ~ 20 times higher number of recorded AE hits per mg Si [13]. Considering that the AE acquisition parameters are nearly the same for both studies, this may be explained by the shorter distance between the AE sensor and the Si electrode in their coin-type cell (estimated at a few millimeters) compared to $\sim 5 \text{ cm}$ for the present Swagelok-type cell in which a

higher fraction of the less energetic AE events must be lost before reaching the sensor. The fact that the Si particles are much smaller in the present work ($\sim 2 \mu\text{m}$ vs $\sim 130 \mu\text{m}$), and thus less sensitive to fracturing may also induce a lower AE activity. Note that the numerous cracks produced in the electrode film during the first cycle (Fig. 3c) may also affect the propagation of the acoustic waves through the electrode, which can decrease the number of AE signals detected beyond the first cycle. As the AE signals are mainly detected during the first cycle, analyses presented below have been focused on this cycle.

3.3. Evolution of electrode potential and acoustic activity during the first cycle

Typical concomitant evolutions of the cumulated acoustic activity and electrode potential during the first discharge and charge are presented in Fig. 5a and c, respectively. The corresponding differential capacity plots (dQ/dV vs V) are shown in Fig. 5b and d.

During the discharge (Fig. 5a and b), a small AE activity (~ 15 hits) is observed at the beginning, i.e. between 1 and $\sim 0.25 \text{ V}$, corresponding to a discharge capacity of about 100 mAh g^{-1} . This can be related to the SEI formation generating AE signals due to the organic film deposition and/or to the release of gas bubbles (e.g. C_2H_4) resulting from the solvent decomposition [19]. Acoustic activity related to the SEI formation was also detected on graphite electrodes for Li-ion batteries [10]. A slow decrease of the potential is then observed between ~ 0.25 and $\sim 0.1 \text{ V}$, which is attributed to the reduction of the native SiO_2 layer present on the Si particles,

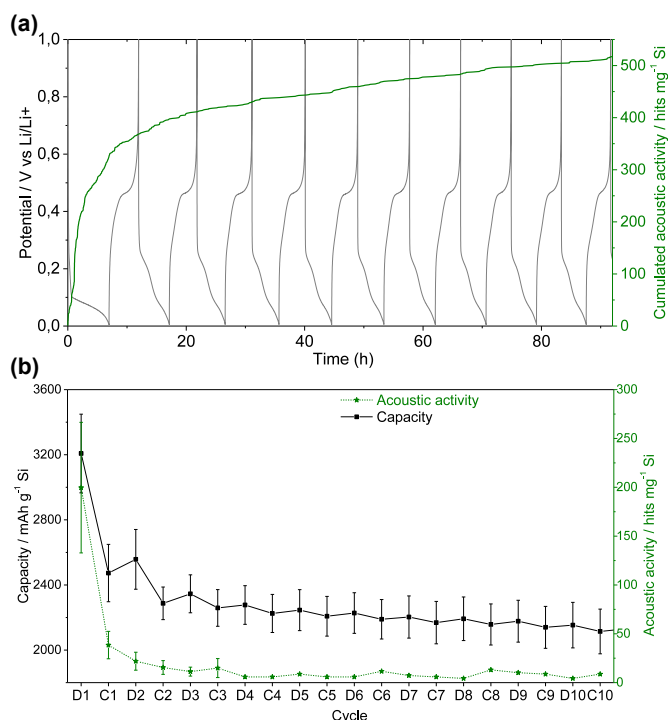


Fig. 4. (a) Typical evolution of the cumulated acoustic activity and electrode potential during the first 10 cycles. (b) Evolution of the electrode capacity and acoustic activity with cycling (mean values based on 8 experiments).

leading to the formation of lithium silicates and Li₂O [20,21]. Almost no AE activity is detected in this potential zone.

When the plateau potential related to the Si lithiation is reached at ~0.13 V, an abrupt increase of the AE activity is observed. Assuming that this AE activity mainly originates from cracking events, this suggests that significant Si particle cracking occurs in the initial stage of the lithiation reaction. This is in accordance with a lithiation occurring through a core–shell mechanism as shown from *ex-situ* Auger Electron Spectroscopy (AES) [22] and *in-situ* TEM [23] observations. According to this model, Si lithiation starts with the formation of an amorphous Li-rich shell surrounding a core of pure crystalline Si. The thickness of this shell increases upon lithiation with a constant composition estimated from AES analyses to be Li_{3.1}Si, at least until a discharge capacity of 1800 mAh g⁻¹ is reached [22]. As shown from *in-situ* TEM observations on Si particles (~1 μm diam.), when the Li_xSi shell reaches a critical thickness of ~150 nm within 2–3 min of discharge, cracks nucleate at the Si particle surface and propagate inward quickly as the lithiation continues. The growth of multiple cracks at different locations on the particle eventually leads to its fracture into several pieces [23]. Thus, the subsequent more progressive increase of the AE activity observed between ca. 0.1 and 0.06 V (~350–2400 mAh g⁻¹) in Fig. 5a and b could originate from the crack growth across the particles resulting in their fracturing into smaller pieces and also to the formation of cracks in the composite film as observed by SEM (Fig. 3b).

A last jump in the acoustic activity is detected at the end of the discharge when the potential reaches ~60 mV. At this potential, it is well known that amorphous Li_xSi is transformed into a crystalline Li₁₅Si₄ phase, which accentuates capacity fading due to inhomogeneous volume change [24]. Thus, the increase of the AE activity detected at this potential may reflect the accentuation of the Si particle and/or film cracking due to this inhomogeneous volume change. Note that this is only observed during the first discharge

(see Fig. 4a) whereas the a-Li_xSi to c-Li₁₅Si₄ phase transition occurs at each cycle, which means that these AE signals do not originate from the phase transition itself but from the resulting electrode cracking occurring essentially during the first discharge.

During the charge (Fig. 5c and d), the AE activity is about 5 times less intense than for the discharge, confirming that the cracks are mainly formed during the lithiation process. This is in contradiction with a recent mechano-electrochemical modeling study, which predicts more mechanical degradation of the active particles during delithiation than during the lithiation process [25]. This result also means that the enlargement of the cracks observed in the film due to its volume contraction during the delithiation of the electrode (Fig. 3c) produces limited detectable AE events, probably because of their low energy. As highlighted in the differential capacity plot (Fig. 5d), the AE activity is significantly accentuated when the potential reaches ~0.45 V, corresponding to the delithiation of the crystalline Li₁₅Si₄ phase which is characterized by an intense and narrow peak in the delithiation dV/dQ curve [24,26]. This is an additional confirmation of the significant effect of the c-Li₁₅Si₄ phase on the electrode cracking process.

3.4. Clustering of the AE signals

As shown in the previous section, AE events detected during the Si electrode cycling can originate from different phenomena: the SEI formation, the surface cracking of the Si particles, their fracturing into smaller pieces and the formation of cracks in the composite film. The assignment of the AE events has been based on their potential zone of production extracted from the concomitant electrochemical measurements, supported by SEM observations and literature data. Since the AE signals are produced by different phenomena, their acoustic characteristics may significantly differ and could be used to separate them. Thus, in the present section, the AE signals are separated on the basis of their characteristic parameters (rise time, duration, amplitude, peak frequency ...).

From the PCA and unsupervised (statistical) clustering procedure, the AE signals detected during the first two cycles can be separated into three different populations. Fig. 6 presents these three populations according to the three principal components, showing their rather good separation. In order to confirm and refine this statistical clustering, a partition has been performed manually by visual examination of the shape of the waveform and power spectrum for each AE signal detected during the first two cycles. Note that about 30% of the AE signals were not classified because they show no evident distinctive characteristics or because they appear as noise events. Three types of signals are then clearly identified, in accordance with the statistical clustering. Their respective typical waveform and power spectra are presented in Fig. 7a–c. Type 1 signals (Fig. 7a), which represent ~50% of the classified signals, are a succession of very short waveform packets with high peak frequency (~700 kHz) and low to medium amplitude. Type 2 signals (Fig. 7c), representing ~30% of the classified signals, display medium peak frequencies (~400 kHz) and some of them are very energetic. Type 3 signals (~20% of the classified signals) have a low peak frequency (~200 kHz), a small number of counts and the lowest energies. The distribution of these three types of AE signals along with their peak frequency, count number and energy is displayed in Fig. 8. The mean values and standard deviations of their acoustic characteristics are indicated in Table 2. It appears clearly that the most discriminative acoustic parameter is the peak frequency.

The typical evolution during the first discharge of the AE activity related to each type of AE signal is shown in Fig. 9. Type 1 signals are mainly detected at the beginning of discharge, i.e. during the SEI formation and upon the initial stage of the Si lithiation. As

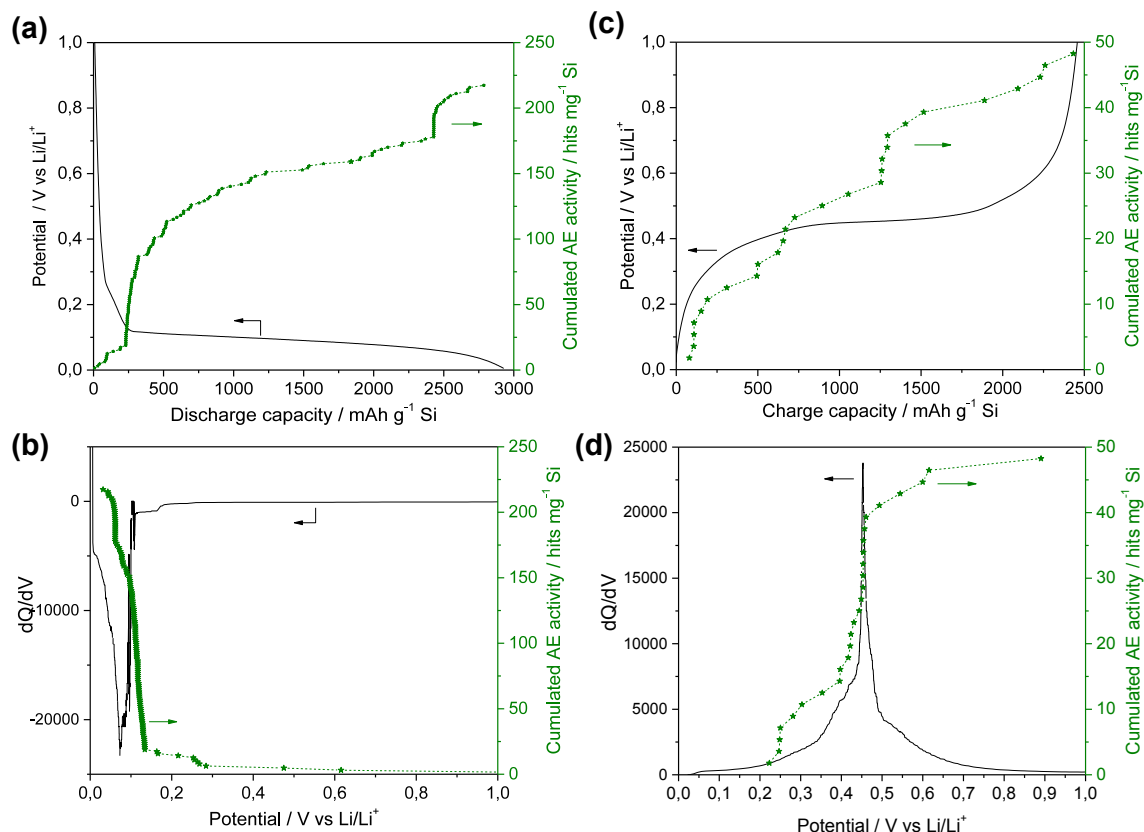


Fig. 5. Typical evolution of the cumulated acoustic activity and electrode potential during the first (a) discharge and (c) charge. The corresponding differential capacity plots (dQ/dV vs V) are shown in (b) and (d).

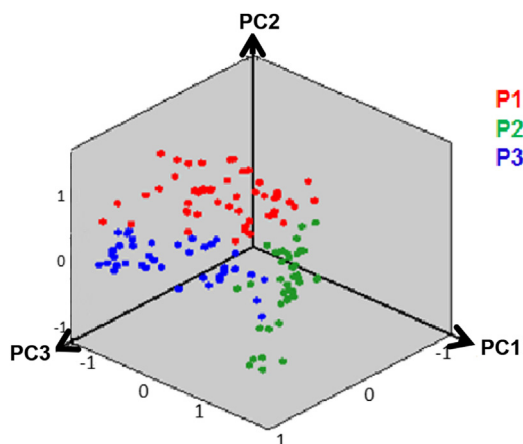


Fig. 6. Distribution along the three principal components of the P1, P2 and P3 populations identified from statistical clustering of the AE signals detected during the first two cycles.

previously discussed, the AE signals related to the SEI formation could originate from the organic film deposition and/or the release of gas bubbles. Usually, AE signals generated by gas evolution exhibit a limited frequency component in the 100–200 kHz range and a long rise time (up to 200 μ s) [7,9]. Such AE signals are not present in the type 1 population, which is characterized by a high peak frequency (\sim 700 kHz) and a short rise time (\sim 15 μ s) (see Table 2). This suggests that the AE signals detected in the SEI potential zone may be generated by the release of stress caused by the

film deposition (e.g. Li₂CO₃) as detected during the deposition of calcium carbonate [27] or zinc phosphate [28]. This may reflect the low gas evolution on a Si-based anode compared to a graphite anode as shown from differential electrochemical mass spectroscopy (DEMS) analysis [19]. However, AE signals due to gas evolution cannot be fully excluded considering the very large frequency range of the type 1 population, as shown in Fig. 7a.

As shown in Fig. 9, a large part of the AE signals detected in the initial stage of the Si lithiation are also of type 1. As discussed previously, the AE signals detected in this zone are assumed to mainly originate from the formation of microcracks at the surface of the Si particles according to the core–shell model of the lithiation process. This is in good agreement with the acoustic characteristics of type 1 signals. Indeed, the fact that this type of signal consists of a succession of very short waveform packets with high peak frequency and low to medium amplitude (Fig. 7a) is compatible with the fast formation of multiple short cracks at the surface of the Si particles. AE signals characterized by a large frequency component including high frequency events were also detected upon stress corrosion cracking (SCC) experiments of metallic samples and were associated with surface cracking process [29]. SEI formation may also occur in this potential zone due to the creation of fresh surfaces with the formation of microcracks at the surface of the Si particles. Unfortunately, on the basis of the present clustering procedure, the resulting AE signals cannot be differentiated from those produced by the particle surface cracking since both phenomenon display type 1 AE signals. Their number is, however, assumed to be minor compared to the amount of AE hits produced by the Si particle cracking.

Type 2 signals are detected all during the Si lithiation process

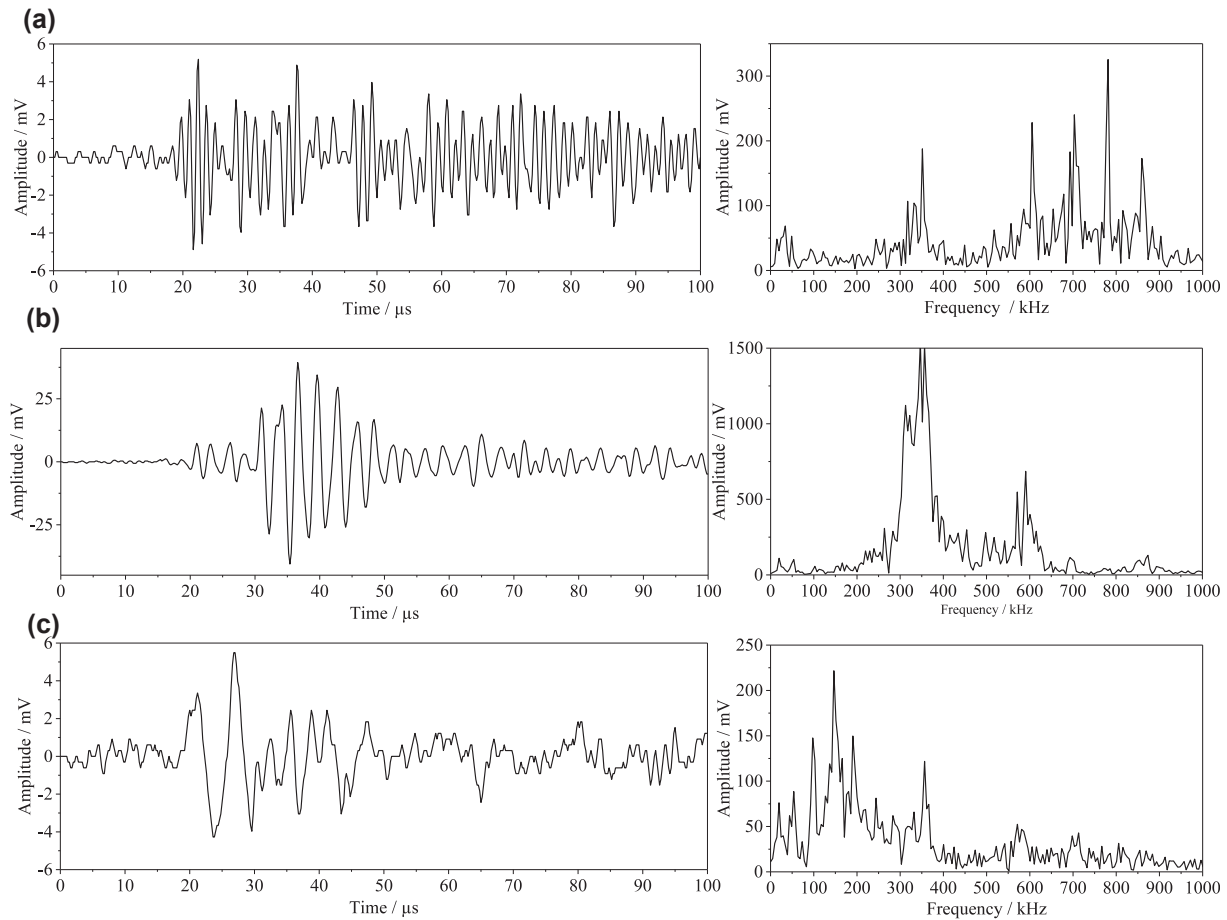


Fig. 7. Typical waveforms and FFT spectra of the AE signals of (a) type 1, (b) type 2 and (b) type 3.

(Fig. 9). Considering their lower peak frequency and higher energy than type 1 signals (Table 1), they could originate from the growth of larger/longer cracks across the particles and/or to the formation of cracks in the composite film. Both phenomena can explain that the cumulative activity of the type 2 signals progresses by sudden jumps during the electrode lithiation due to some inhomogeneity

in the mechanical resistance of the film and in the Si particle size. These activity jumps may also result from well-known avalanche phenomena, where the rupture of a strong bond induces the rupture of all the weak bonds around it [25]. Similar AE waveforms related to particle cracking were detected during the electrochemical hydrogenation of metal hydrides for Ni–MH batteries [6]. They were also observed during tensile tests of fiberglass and was attributed to the matrix cracking [30].

Regarding the type 3 signals in Fig. 9, their cumulated activity is much lower than for type 1 and type 2 signals and increases when the electrode potential reaches 60 mV, corresponding to the formation of the $c\text{-Li}_{15}\text{Si}_4$ phase as previously discussed. Their lower values in terms of counts, duration, energy and peak frequency compared to those of type 1 and type 2 signals (Table 2) suggest that they could correspond to the completion of particle/film cracking initiated at lower lithiation state.

4. Conclusion

This study has shown that the AE technique is a suitable analytical tool for monitoring the morphological degradation of Si-based anodes upon cycling. On the basis of the evolution of the AE activity as a function of the electrode potential and cycle number and by clustering the AE signals according to their acoustic characteristics, it was shown that:

- The electrode cracking mainly occurs during the first discharge (lithiation).

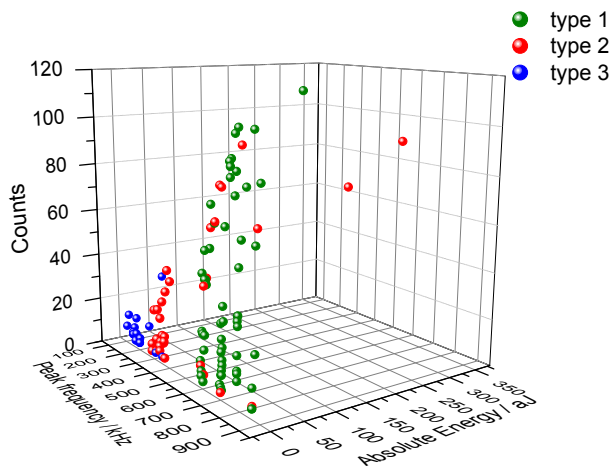


Fig. 8. Distribution as a function of their frequency, number of counts and energy of the three types of signals identified from manual clustering of the AE events detected during the first two cycles.

Table 2

Mean and standard deviation values of the acoustic parameters of the type 1, type 2 and type 3 AE signals detected during the first two cycles.

	Type 1		Type 2		Type 3	
	Mean	Std	Mean	Std	Mean	Std
Rise time (μ s)	15.0	13.0	11.9	8.1	6.8	2.4
Counts to peak	7.6	7.3	4.7	3.4	1.8	0.4
Counts	41.0	32.4	28.9	27.3	7.1	6.6
Duration (μ s)	128.4	52.8	106.3	64.1	67.2	62.2
Amplitude (dB)	36.9	5.2	39.1	8.0	35.5	3.4
Absolute energy (aJ)	9.0	15.1	36.6	85.8	3.8	7.4
Peak frequency (kHz)	705.2	87.4	424.2	148.4	183.7	62.0

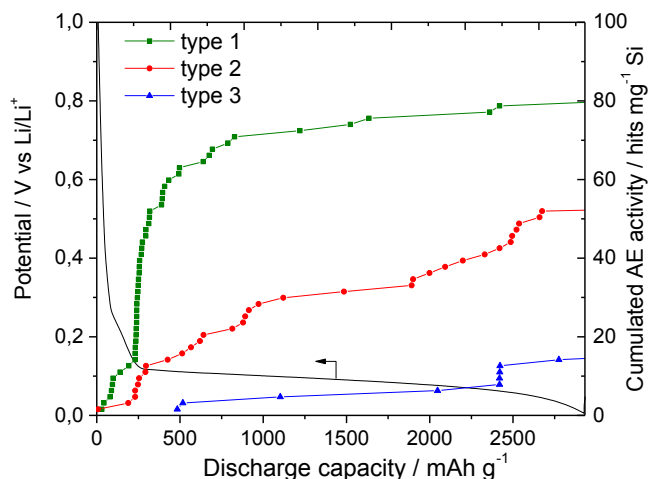


Fig. 9. Evolution of the electrode potential and acoustic activity of type 1, 2 and 3 signals during the first discharge.

- The SEI formation is not very acoustically emissive, which may reflect the low gas evolution upon its formation.
- Si particle cracking is initiated in the early stage of the lithiation, in good agreement with a core-shell lithiation mechanism.
- The electrode cracking is accentuated in both discharge and charge by the presence of the $c\text{-Li}_{15}\text{Si}_4$ phase.
- The enlargement of the cracks occurring in the composite film during the electrode contraction (charge) is not clearly detected by AE, probably because of the low energy of the produced signals.
- On the basis of the present AE signal clustering, it appears difficult to clearly differentiate the AE signals originating from the SEI formation to those produced by the particle surface cracking. This is also true for the AE signals due the particle bulk fracturing and those due to the film cracking. To resolve this issue, further work is planned and will consist of analyzing the

dependence on the AE responses of the Si particle size, Si loading, binder composition, electrolyte composition, etc.

Acknowledgments

The authors thank the Rhône-Alpes region, France, and the Natural Sciences and Engineering Research Council (NSERC) of Canada for supporting this work.

References

- [1] M.N. Obrovac, L.J. Krause, *J. Electrochem. Soc.* 154 (2007) A103–A108.
- [2] J.H. Ryu, J.W. Kim, Y.-E. Sung, S.M. Oh, *Electrochem. Solid State Lett.* 7 (2004) A306–A309.
- [3] Y. Oumellal, N. Delpuech, D. Mazouzi, N. Duprée, J. Gaubicher, P. Moreau, P. Soudan, B. Lestriez, D. Guyomard, *J. Mater. Chem.* 21 (2011) 6201–6208.
- [4] D. Mazouzi, N. Delpuech, Y. Oumellal, M. Gauthier, M. Cerbelaud, J. Gaubicher, N. Dupré, P. Moreau, D. Guyomard, L. Roué, B. Lestriez, *J. Power Sources* 220 (2012) 180–184.
- [5] American Society of Nondestructive Testing (ASNT), *Nondestructive Testing Handbook*, in: *Acoustic Emission Testing*, third ed., vol. 6, 2005, Columbus, OH.
- [6] H. Inoue, R. Tsuzuki, S. Nohara, C. Iwakura, *Electrochem. Solid State Lett.* 9 (2006) A504–A506.
- [7] A. Etienne, H. Idrissi, L. Roué, *J. Power Sources* 196 (2011) 5168–5173.
- [8] T. Ohzuku, H. Tomura, K. Sawai, *J. Electrochem. Soc.* 144 (1997) 3496–3500.
- [9] T. Matsuo, M. Uchida, H. Cho, *J. Solid Mech. Mater. Eng* 5 (2011) 678–689.
- [10] N. Kircheva, S. Genies, D. Brun-Buisson, P.-X. Thivel, *J. Electrochem. Soc.* 159 (2012) A18–A25.
- [11] C. Villeveille, M. Boinet, L. Monconduit, *Electrochem. Commun.* 12 (2010) 1336–1339.
- [12] N. Kircheva, S. Genies, C. Chabrol, P.-X. Thivel, *Electrochim. Acta* 88 (2013) 488–494.
- [13] A. Rhodes, N. Dudney, E. Lara-Curzio, C. Daniel, *J. Electrochem. Soc.* 157 (2010) A1354–A1360.
- [14] K. Rhodes, M. Kirkham, R. Meisner, C.M. Parish, N. Dudney, C. Daniel, *Rev. Sci. Instrum.* 82 (2011) 075107-1/7.
- [15] S. Kalnaus, K. Rhodes, C. Daniel, *J. Power Sources* 196 (2011) 8116–8124.
- [16] D. Mazouzi, L. Roué, D. Guyomard, B. Lestriez, *Electrochem. Solid State Lett.* 12 (2009) A215–A218.
- [17] H. Abdi, L.J. Williams, *Wiley Interdiscip. Rev. Comput. Stat.* 2 (2010) 433–459.
- [18] E. Radvanyi, W. Porcher, E. De Vito, A. Montani, S. Franger, S. Jouanneau Si Larbi, *Phys. Chem. Chem. Phys.* 16 (2014) 17142.
- [19] M. Holzapfel, H. Buqa, L.J. Harwick, M. Hahn, A.A. Würsig, W. Scheifele, P. Novák, R. Kötz, C. Veit, F.-M. Petrat, *Electrochim. Acta* 52 (2006) 973–978.
- [20] E. Radvanyi, E. De Vito, W. Porcher, S. Jouanneau Si Larbi, *J. Anal. At. Spectrom.* 29 (2014) 1120–1131.
- [21] T. Kim, S. Park, S.M. Oh, *J. Electrochem. Soc.* 154 (2007) A1112–A1117.
- [22] E. Radvanyi, E. De Votto, W. Porcher, J. Danet, P. Desbois, J.-F. Colin, S. Jouanneau Si Larbi, *J. Mater. Chem. A* 1 (2013) 4956–4965.
- [23] X.H. Liu, L. Zhang, S. Huang, S.X. Mao, T. Zhu, J.Y. Huang, *ACS Nano* 6 (2012) 1522–1531.
- [24] J. Li, J.R. Dahn, *J. Electrochem. Soc.* 154 (2007) A156–A161.
- [25] P. Barai, P.P. Mukherjee, *J. Electrochem. Soc.* 161 (2014) F3123–F3136.
- [26] V.L. Chevrier, L. Liu, B.B. Le, J. Lund, B. Molla, K. Reimer, L.J. Krause, L.D. Jensen, E. Figgemeir, K.W. Eberman, *J. Electrochem. Soc.* 161 (2014) A783–A791.
- [27] S. Ramadan, H. Idrissi, *Desalination* 219 (2008) 358–366.
- [28] F. Simescu, H. Idrissi, *Meas. Sci. Technol.* 20 (2009) 055702.
- [29] A. Proust, H. Mazille, P. Fleischmann, R. Rothea, *J. Acoust. Emiss.* 19 (2001) 229–240.
- [30] V. Arumugam, C. Suresh Kumar, C. Santulli, F. Sarasini, A. Joseph Stanley, *J. Test. Eval.* 39 (2011) 954–966.